Volume 26
Number 35
21 September 2024
Pages 22813–23508

PCCP

Physical Chemistry Chemical Physics

rsc.li/pccp

25 YEARS ANNIVERSARY

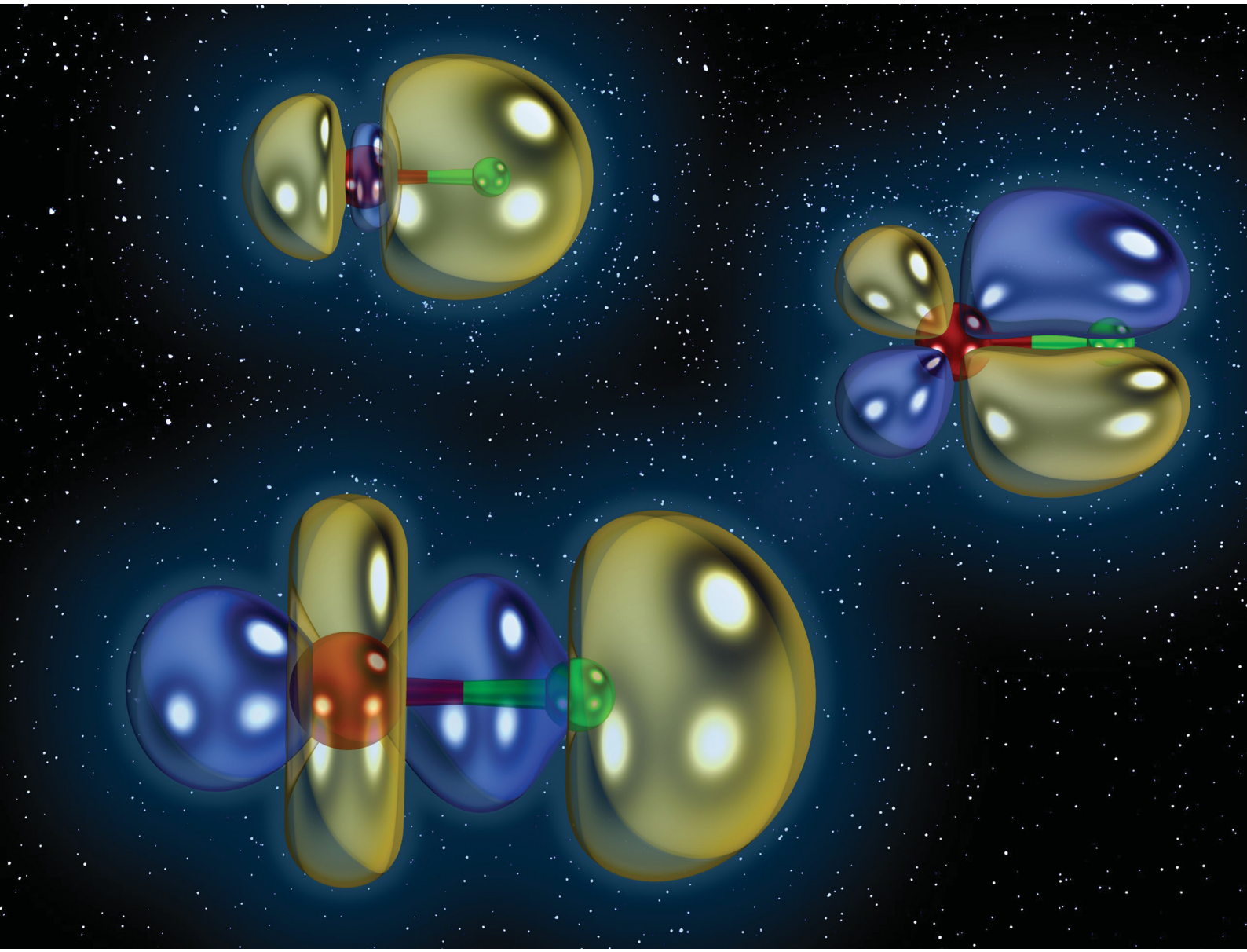

ISSN 1463-9076

ROYAL SOCIETY OF CHEMISTRY

PAPER

Isuru R. Ariyarathna

Wavefunction theory and density functional theory analysis of ground and excited electronic states of TaB and WB

PCCP Owner Societies

PCCP

PAPER

View Article Online
View Journal | View Issue

Cite this: *Phys. Chem. Chem. Phys.*, 2024, **26**, 22858

Wavefunction theory and density functional theory analysis of ground and excited electronic states of TaB and WB†

Isuru R. Ariyarathna

Received 28th May 2024,
Accepted 25th July 2024

DOI: 10.1039/d4cp02202e

rsc.li/pccp

Several low-lying electronic states of TaB and WB molecules were studied using *ab initio* multireference configuration interaction (MRCI), Davidson corrected MRCI (MRCI+Q), and coupled cluster singles doubles and perturbative triples [CCSD(T)] methods. Their full potential energy curves (PECs), equilibrium electron configurations, equilibrium bond distances (r_es), dissociation energies (D_es), excitation energies (T_es), harmonic vibrational frequencies (ω_es), and anharmonicities ($\omega_e x_e$s) are reported. The MRCI dipole moment curves (DMCs) of the first 5 electronic states of both TaB and WB are also reported and the equilibrium dipole moment (μ) values are compared with the CCSD(T) μ values. The most stable $1^3\Pi$ ($1\sigma^2 2\sigma^2 3\sigma^1 1\pi^3$) and $1^5\Delta$ ($1\sigma^2 2\sigma^2 3\sigma^1 1\pi^2 1\delta^1$) electronic states of TaB lie close in energy with ~62 kcal mol^{-1} D_e with respect to the Ta(^{4}F) + B(^{2}P) asymptote. However, spin–orbit coupling effects make the $1^5\Delta_{0^+}$ state the true ground state of TaB. The ground electronic state of WB ($1^6\Pi$) has the $1\sigma^2 2\sigma^1 3\sigma^1 1\pi^3 1\delta^2$ electron configuration and is followed by the excited $1^6\Sigma^+$ and $1^4\Delta$ states. Finally, the MRCI D_e, r_e, ω_e, and $\omega_e x_e$ values of the $1^3\Pi$ state of TaB and $1^6\Pi$ and $1^4\Delta$ states of WB are used to assess the density functional theory (DFT) errors on a series of exchange–correlation functionals that span multiple-rungs of the Jacob's ladder of density functional approximations (DFA).

I. Introduction

A fundamental understanding of the electron distribution of atoms and small molecules provides us with valuable information on their properties that are vital for the progression of many disciplines of science such as catalysis, surface science, synthetic chemistry, astrophysics, and plasma science. For this topic, experimental spectroscopic studies and computational explorations have become quite indispensable avenues for gaining useful insight into electronic structures of molecules and for predicting their reactivities.[1–8] Indeed, many experimental spectroscopic analyses are conjoined with theoretical predictions for resolving and understanding spectral features.[1–4,6,7] However, it should be noted that both spectroscopic and high-level *ab initio* studies of small molecular species are highly challenging to perform and requires a great deal of experimental and theoretical expertise.[1,2,9–13]

So far, many attempts have been made to understand the electronic spectra of diatomic molecular species. In particular, the main focus has been on transition metal (TM) monoxides and mononitrides due to their applications in catalysis and surface science (see ref. 9, 10, 14 and 15 and references therein). Interestingly, only a few such attempts have been made on 1st and 2nd row TM monoborides,[16–31] and even less for 3rd row TM monoborides, likely due to their strong relativistic effects.[12,24,25,31–37] Consequently, a high-level theoretical analysis of TaB has not yet been explored. Hence a part of the present work is devoted to analyzing *ab initio* electronic structures of the TaB molecule. Furthermore, a series of excited electronic states of its neighboring monoboride WB was also analyzed.

Recently, a resonant two-photon ionization spectroscopic analysis was performed by the Morse group to measure the bond dissociation energies of several early TM borides including TaB and WB.[31] Their measured D_0 values of TaB and WB are 2.700(3) and 2.730(4) eV, respectively. Importantly, this is the only experimental spectroscopic analysis reported so far for early TM monoborides. They further performed DFT/B97-1 (with the aug-cc-pVTZ-PP of Ta/W and cc-pVTZ of B basis set) analysis and

Physics and Chemistry of Materials (T-1), Los Alamos National Laboratory, Los Alamos, NM 87545, USA. E-mail: isuru@lanl.gov

† Electronic supplementary information (ESI) available: Table S1 lists MRCI T_e and experimental T_e values of Ta atom; Table S2 lists MRCI findings of spin–orbit states of TaB; Table S3 lists DFT findings of TaB($1^3\Pi$); Table S4 lists % DFT errors of various properties of Tab($1^3\Pi$); Table S5 lists MRCI T_e and experimental T_e values of W atom; Table S6 lists the % compositions of spin–orbit states of WB; Table S7 lists DFT findings of WB($1^6\Pi$) and WB($1^4\Delta$); Tables S8 and S9 list % DFT errors of various properties of Wb($1^6\Pi$) and Wb($1^4\Delta$); Fig. S1 and S2 illustrate the CASSCF PECs of TaB and WB; Fig. S3 illustrates the DFT D_e of WB($1^4\Delta$). See DOI: https://doi.org/10.1039/d4cp02202e

predicted $^5\Delta$ and $^6\Sigma^+$ ground states for TaB and WB with D_0 values of 2.95 and 2.89 eV, respectively. Furthermore, for TaB they observed $^3\Pi$ and $^3\Sigma^+$ states lying 0.07 and 0.5 eV above the $^5\Delta$ of TaB. A DFT/B3LYP (with the LANL2DZ basis set) study reported prior to the work by the Morse group (by Kalamse *et al.*) has identified this $^3\Sigma^+$ as the ground state of TaB with a binding energy of 2.49 eV.[38] Furthermore, the same DFT study by Kalamse *et al.*, predicted a $^6\Sigma^-$ ground electronic state for WB with a binding energy of 2.77 eV.[38] The only high-level *ab initio* study available for WB is the work by Melo and Dixon, which predicted a $^6\Pi$ ground state for the WB which is followed by the $^6\Sigma^+$ and $^4\Delta$ excited electronic states.[12] Of course, the spin–orbit effects are expected to be strong for heavy WB and the inclusion of spin–orbit coupling effects at the CASPT2 (complete active space second-order perturbation theory) level has produced a $^6\Pi_{7/2}$ spin–orbit ground state for the molecule with a 2.67 eV D_0 which is in harmony with the experimental value reported by the Morse group.[12,31]

Ab initio multireference methods provide accurate predictions for molecular systems with complicated electronic structures.[39,40] In particular, the widely accepted MRCI is an ideal method of choice to analyze the excited states of highly correlated systems with dense electronic spectra.[41–45] This is due to the fact that many excited electronic states of various molecular systems are multireference in nature and their wavefunctions prevail by more than one dominant electronic configuration. However, achieving appropriate convergence criteria for multireference calculations is challenging and hence they are markedly less popular. Furthermore, high-level multireference analysis requires a substantial amount of computing power and the calculations are only feasible for small molecular systems containing only a few atoms. On the other hand, approximate DFT is a popular method being used to gain insight into many chemical phenomena due to its favorable accuracy–efficiency compromise.[46–50] Indeed, its user-friendly black box nature is rather alluring. Of course, DFT has become quite imperative for predicting properties of larger molecular complexes and solids, where the implementation of expensive wavefunction theories (WFT) is not yet possible. However, DFT predictions are susceptible to being influenced by the exchange–correlation functional utilized and are known to be system and property dependent.[37,51,52] This complicates the application of DFT and its reliability. In principle we would expect better predictions from more expensive functionals that belong to higher rungs of the Jacob's ladder of DFA[53] compared to the less expensive functionals at the lower rungs. However, climbing up the Jacob's ladder of DFA does not guarantee improvements to the accuracy of the predictions especially for highly correlated TM-based systems that are known to be affected by static correlation errors and delocalization errors.[37,51] Hence, often the selection of an appropriate functional to represent a system and a property is followed by DFT benchmark studies.

The current work analyzes 10 and 14 low-lying electronic states of TaB and WB respectively. Their full PECs, electronic configurations, D_es, r_es, T_es, ω_es, $\omega_e x_e$s, and μ values are reported by means of MRCI,[54–56] MRCI+Q, and CCSD(T)[57] levels of theory with correlation consistent basis sets. The D_es, r_es, ω_es, and $\omega_e x_e$s values of three low energy single-reference electronic states of TaB and WB are also calculated with a set of exchange–correlation functionals that falls under multiple-rungs of the Jacob's ladder of DFA[53] and the DFT errors were assessed with respect to the WFT findings.

II. Computational details

WFT and DFT calculations were performed utilizing MOLPRO 2023.2[58–60] and Gaussian 16[61] quantum chemistry packages, respectively. First, full PECs of ground and several excited electronic states of TaB and WB were produced under the internally contracted MRCI method[54–56] with the quadruple-ζ quality correlation consistent cc-pVQZ basis set of B and cc-pVQZ-PP set of Ta and W.[62,63] The Stuttgart relativistic pseudopotentials that represent $1s^22s^22p^63s^23p^64s^23d^{10}4p^64d^{10}4f^{14}$ electrons were used (ECP60) for Ta and W atoms.[63] All MRCI calculations were performed on top of complete active space self-consistent field (CASSCF)[64–67] reference wavefunctions (WFs). The CASSCF wavefunctions of TaB and WB were generated by allocating 8 and 9 electrons, respectively, to 13 orbitals [*i.e.*, CAS(8,13) and CAS(9,13)]. At the dissociating limit, the 13 active orbitals are purely 6s, 6p, and 5d atomic orbitals of the metal atom (M = Ta/W) and 2s and 2p atomic orbitals of B. Under the utilized C_{2v} Abelian sub point group, the active orbitals are $6a_1$ (6s, $5d_{z^2}$, $5d_{x^2-y^2}$, and $6p_z$ of M and 2s and $2p_z$ of B), $3b_1$ ($5d_{xz}$ and $6p_x$ of M and $2p_x$ of B), $3b_2$ ($5d_{yz}$ and $6p_y$ of M and $2p_y$ of B), and $1a_2$ ($5d_{xy}$ of M). At the CASSCF level a series of PECs arising from Ta(^{4}F) + B(^{2}P), Ta(^{4}P) + B(^{2}P), and Ta(^{2}G) + B(^{2}P) combinations were studied. At the proceeding MRCI level, the PECs of the lowest 10 molecular electronic states of TaB were produced. For WB, at the CASSCF level, all PECs of W(^{7}S) + B(^{2}P), W(^{5}D) + B(^{2}P), and W(^{3}P) + B(^{2}P) and several PECs of W(^{3}H) + B(^{2}P) were investigated but only the PECs of the 14 lowest energy states of WB were investigated at the MRCI level. In all MRCI calculations, single and double electron promotions from active space to virtual space were allowed.

To obtain more accurate energetics and spectroscopic parameters, another set of MRCI calculations were performed around the equilibrium bond distance region by including only 10 (of TaB) and 14 (of WB) states at the CASSCF and MRCI level. For these calculations the same quadruple-ζ quality basis set was used. Davidson correction (MRCI+Q) was applied as a size-extensivity correction. The numerical values of MRCI and MRCI+Q PECs were used to solve the ro-vibrational Schrödinger equation to calculate ω_e and $\omega_e x_e$ values. Similarly, the minima of the PECs were used to calculate T_es, r_es, and D_es. Specifically, the D_es of molecular electronic states were calculated with respect to Ta(^{4}F) + B(^{2}P) or W(^{7}S) + B(^{2}P) fragments that are separated by 200 Å. The reported spin–orbit coupling effects were calculated at the MRCI level by implementing the Breit–Pauli Hamiltonian (more information regarding the spin–orbit analysis is provided in the discussion section). Dipole moment

curves (DMCs) of several low-lying electronic states of TaB and WB were also produced at the MRCI level under the same basis set.

Low-lying single-reference electronic states of TaB were further investigated by performing single-reference CCSD(T)[57] calculations constructed on Hartree–Fock wavefunctions. Two types of CCSD(T) calculations were performed utilizing cc-pVQZ[62] (B) cc-pVQZ-PP (Ta)[63] and aug-cc-pV5Z[68] (B) aug-cc-pV5Z-PP (Ta)[63] basis sets. For simplicity, hereafter, the CCSD(T) calculations carried out with the latter basis set are denoted by A5Z-CCSD(T). Furthermore, another set of CCSD(T) calculations were executed by correlating $5s^25p^6$ core electrons of Ta using the aug-cc-pV5Z[68] (B) aug-cc-pwCV5Z-PP (Ta)[63] basis set [hereafter called A5Z-C-CCSD(T)]. The dipole moment (μ) values of low-lying single-reference electronic states of both TaB and WB were studied at coupled cluster levels using the finite-field approach by applying a field (f) of 0.01 a.u. to the positive and negative directions of the M–B and using the resulting $E(f)$ and $E(-f)$ energies in the $\mu = [E(f) - E(-f)]/2f$ equation.

The single-reference $1^3\Pi$ state of TaB and $1^6\Pi$ and $1^4\Delta$ states of WB were also studied under DFT with a series of exchange–correlation functionals that span several rungs of the Jacob's ladder of DFA.[53] Specifically, semi-local generalized gradient approximation (GGA: BP86,[69,70] BLYP,[71,72] PBE[73]), *meta*-GGA (MGGA: TPSS,[74] MN15-L[75]), global GGA hybrid (B3LYP,[76,77] B3P86,[69,76] B3PW91,[76] PBE0[78,79]), MGGA hybrid (TPSSh,[74] M06,[80] M06-2X,[80] MN15[81]), and range-separated hybrid (RSH: LRC-ωPBE,[82] CAM-B3LYP,[83] ωB97X[84]) functionals were applied. For all DFT calculations, default SCF (self-consistent field) convergence thresholds, grids, and frozen core settings implemented in Gaussian 16 were utilized. In each case, stable = opt Gaussian keyword was used to obtain stable wavefunctions. The cc-pVQZ (B) cc-pVQZ-PP (Ta) basis set was used for all DFT calculations.

III. Results and discussion

III.A. TaB

The MRCI constructed on top of CASSCF WFs accounts for a large fraction of the dynamic electron correlation and hence the results of this method are highly reliable. In particular, this technique is well known for producing accurate potential energy profiles of the ground and electronically excited states of highly correlated diatomic molecular species.[10,37,41–43]

In the present work, first, we have analyzed the electronic states of Ta and B atoms to gain insight into the molecular electronic states that they form. Ta has a ^{4}F ground electronic term with the $5d^36s^2$ valence electronic configuration. Its first two electronically excited states (*i.e.*, ^{4}P and ^{2}G) lying at 17.3–26.5 and 27.7–30.6 kcal mol^{-1} have the same electron arrangement as the ground states.[85] The electronic spectrum of Ta is highly complicated beyond the ^{2}G state due to a series of closely arranged states (see the experimental excitation energies listed in ref. 85). Hence, here we have selected the low-lying ^{4}F, ^{4}P, and ^{2}G electronic states of Ta to investigate their reactions with a B atom. The ground state of the B atom is a ^{2}P with the

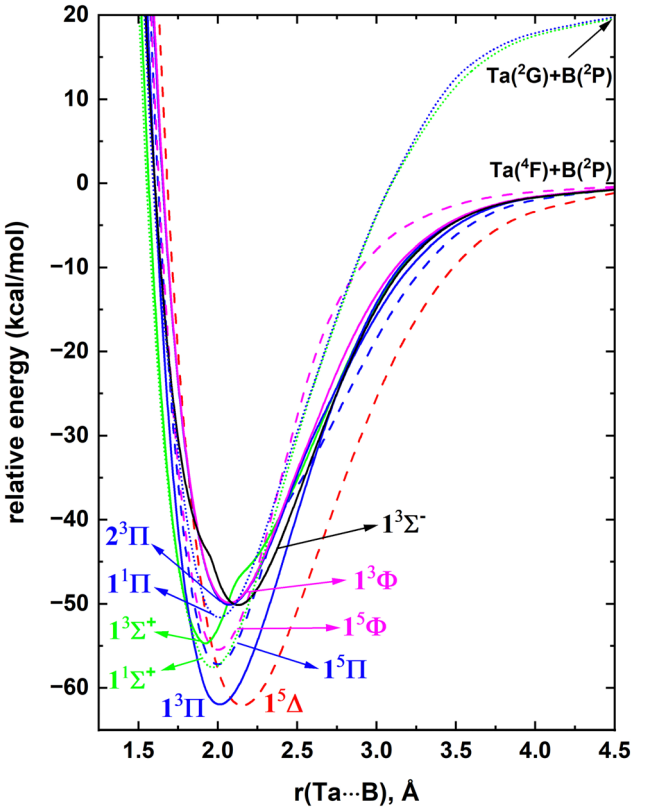

Fig. 1 Full MRCI PECs of TaB as a function of Ta···B distance [r(Ta···B), Å]. The relative energies are referenced to the total energy of the Ta(^{4}F) + B(^{2}P) fragments at r = 200 Å, which is set to 0 kcal mol^{-1}. The Σ^+, Π, Δ, Φ, and Σ^- states are shown in green, blue, red, pink, and black respectively. The solid, dotted, and dashed PECs represent triplet, singlet, and quintet spins, respectively.

[He]$2s^22p^1$ electron configuration. Its first excited state (*i.e.*, ^{4}P; [He]$2s^12p^2$) lies ~82 kcal mol^{-1} above.[85] As B(^{4}P) is comparatively high in energy, its interactions with Ta were not considered. The selected reactants in the present work are Ta(^{4}F) + B(^{2}P), Ta(^{4}P) + B(^{2}P), and Ta(^{2}G) + B(^{2}P). Specifically, we have investigated the 21(quintet + triplet) and 9(quintet + triplet) PECs originating from Ta(^{4}F) + B(^{2}P) and Ta(^{4}P) + B(^{2}P) respectively and the 27 singlet-spin PECs originating from the Ta(^{2}G) + B(^{2}P) asymptote (ESI,† Fig. S1). As shown in the ESI† Fig. S1, the electronic spectrum of TaB is dense and highly complicated, hence only the 10 lowest lying molecular electronic states of TaB were investigated at the MRCI level. The MRCI PECs of TaB are given in Fig. 1. The electronic states arising from the Ta(^{4}P) + B(^{2}P) asymptotes are not among the 10 most stable electronic states of TaB and hence they are not shown in Fig. 1. Note that only two singlet spin electronic states originating from Ta(^{2}G) + B(^{2}P) fall among the 10 reported states of TaB. The two most stable electronic states of TaB (*i.e.*, $1^3\Pi$ and $1^5\Delta$) dissociate into Ta(^{4}F) + B(^{2}P) fragments, and have ~62 kcal mol^{-1} D_e. Similar to the Ta atom, the excited electronic spectrum of TaB is complicated with a set of closely arranged electronic states and specifically the 2nd to 10th excited states of TaB are assembled within 8 kcal mol^{-1} of energy.

The dominant electron configurations and configuration interaction coefficients collected at the corresponding equilibrium distances of the studied states of TaB are listed in Table 1. The contours of the state-average CASSCF active orbitals obtained at the r_e = 2.0 Å are plotted in Fig. 2. The 1σ molecular orbital consists of the dominant 2s of B and minor $5d_{z^2}$ and 6s character of Ta. The 2σ is dominantly the 6s of Ta but bears a small contribution from the 2s of B. The hybridization of the $5d_{z^2}$ of Ta with $2p_z$ of B is shown in the 3σ molecular orbital. Similarly, the $5d_{xz}$(Ta) + $2p_x$(B) and $5d_{yz}$(Ta) + $2p_y$(B) combinations give rise to the perpendicular $1\pi_x$ and $1\pi_y$ bonding molecular orbitals. The $1\pi_x$* and $1\pi_y$* antibonding molecular orbitals resulting from $5d_{xz}$(Ta) − $2p_x$(B) and $5d_{yz}$(Ta) − $2p_y$(B) are also present in the active space but not given in Fig. 2 since they are not occupied by the reported states. Due to the symmetry effects, the $5d_{x^2-y^2}$ and $5d_{xy}$ atomic orbitals of Ta do not hybridize with the active orbitals of B and hence directly correlate to the $1\delta_{x^2-y^2}$ and $1\delta_{xy}$ orbitals of Fig. 2.

At the equilibrium distance, the $1^3\Pi$ state has the $1\sigma^2 2\sigma^2 3\sigma^1 1\pi^3$ dominant electronic configuration (Table 1) which accounts for an approximate bond order of 2. Its effective bond order based on the dominant electron configuration is indeed 1.6. The electronic configuration of the $1^5\Delta$ can be produced by transferring an electron from the $1\pi_y$ of $1^3\Pi$ to an 1δ orbital (*i.e.*, $1\sigma^2 2\sigma^2 3\sigma^1 1\pi^2 1\delta^1$). Since the 1δ orbitals are non-bonding, the bond order of the $1^5\Delta$ is ∼1.5. As expected, the lower bond order of the $1^5\Delta$ compared to the $1^3\Pi$ translates to a longer r_e of the former compared to the latter (Fig. 1). The second excited state of the TaB is a $^1\Sigma^+$ with a $1\sigma^2 2\sigma^2 1\pi^4$ electron arrangement with a bond order of 2. Note that the first three electronic states of TaB (*i.e.*, $1^3\Pi$, $1^5\Delta$, $1^1\Sigma^+$) are single-reference in nature and are followed by the multireference $1^5\Pi$ and $1^5\Phi$ states. These two $1^5\Pi$ and $1^5\Phi$ states possess similar electron arrangements that are separated by the $(1\pi_x)^2(1\pi_y)^1 - (1\pi_x)^1(1\pi_y)^2$ and $(1\pi_x)^2(1\pi_y)^1 + (1\pi_x)^1(1\pi_y)^2$ components, respectively (Table 1). An electron transfer from 2σ of $1^1\Sigma^+$ to the 3σ orbital produces the next electronic state of TaB (*i.e.*, $1^3\Sigma^+$). The proceeding $1^1\Pi$ is the corresponding open-shell multireference singlet spin electronic state of the $1^3\Pi$. The lower stability of the low-spin $1^1\Pi$ compared to the $1^3\Pi$ is an example of the preservation of the Hund's rule.

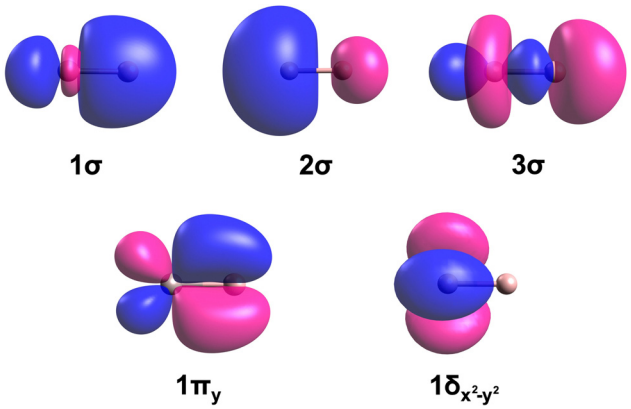

Fig. 2 Select molecular orbitals of TaB. The Ta (left atom) and B (right atom) atoms of each orbital plot are shown in gray and soft-pink colors, respectively. The rotations of $1\pi_y$ by 90° and $1\delta_{x^2-y^2}$ by 45° along the *z*-axis yield the $1\pi_x$ and $1\delta_{xy}$ molecular orbitals, respectively. Blue and pink colors correspond to the negative and positive phases of the molecular orbitals. The contours were produced using the Avogadro software.[86,87] The molecular orbitals of WB have similar shapes.

Table 1 Dominant electronic configurations of the 10 reported electronic states of TaB

State[a]	Coefficient[b]	1σ	2σ	3σ	$1\pi_x$	$1\pi_y$	$1\delta_{x^2-y^2}$	$1\delta_{xy}$
$1^3\Pi$	0.90	2	2	α	α	2	0	0
$1^5\Delta$	0.88	2	2	α	α	α	0	α
$1^1\Sigma^+$	0.88	2	2	0	2	2	0	0
$1^5\Pi$	−0.64	2	α	α	α	2	α	0
	0.64	2	α	α	2	α	0	α
$1^5\Phi$	0.65	2	α	α	α	2	α	0
	0.65	2	α	α	2	α	0	α
$1^3\Sigma^+$	0.87	2	α	α	2	2	0	0
$1^1\Pi$	−0.57	2	2	α	β	2	0	0
	0.57	2	2	β	α	2	0	0
$2^3\Pi$	0.47	2	2	0	2	α	0	α
	−0.46	2	2	0	α	2	α	0
	0.30	2	α	β	2	α	0	α
	−0.30	2	α	β	α	2	α	0
$1^3\Phi$	0.46	2	2	0	2	α	0	α
	0.47	2	2	0	α	2	α	0
	0.25	2	α	β	2	α	0	α
	0.25	2	α	β	α	2	α	0
	−0.27	2	α	α	α	2	β	0
	−0.27	2	α	α	2	α	0	β
$1^3\Sigma^-$	0.75	2	2	2	α	α	0	0

[a] Only B_1 components of Π and Φ states and A_1 of the $1^5\Delta$ under C_{2v} symmetry are listed. [b] Only the configuration interaction coefficients that are equal or larger than 0.25 of the corresponding natural orbital representations are listed.

The CCSD(T) level of theory can represent single-reference electronic states of molecules with high accuracy and hence are adopted to analyze the three lowest energy electronic states of TaB ($1^3\Pi$, $1^5\Delta$, and $1^1\Sigma^+$). The coupled cluster, MRCI, and MRCI+Q D_e, r_e, T_e, ω_e, and $\omega_e x_e$ values of the studied states of TaB are listed in Table 2. The CCSD(T) calculations require less computational resources compared to MRCI and therefore we were able improve the basis set from cc-pVQZ (B) cc-pVQZ-PP(Ta) to aug-cc-pV5Z (B) aug-cc-pV5Z-PP(Ta) to provide more accurate estimates for the properties of TaB. Importantly, at this level using the aug-cc-pV5Z (B) aug-cc-pwCV5Z-PP(Ta) basis set we were able to acquire the correlation of the inner $5s^25p^6$ electrons of Ta which is expected to further improve the accuracy of the predictions. As shown in the potential energy profile (Fig. 1), the $1^3\Pi$ and $1^5\Delta$ states of TaB lie very close in energy and at the MRCI and MRCI+Q levels the former is ∼0.2 kcal mol^{-1} more stable compared to the latter (Table 2). However, this relative stabilization of $1^3\Pi$ over $1^5\Delta$ is within the margin of error of the methods and the basis set, and hence it is difficult to decisively assign the exact ground state for TaB. Indeed, this is true as demonstrated by the 0.7 kcal mol^{-1} stability of $1^5\Delta$ compared to the $1^3\Pi$ at the CCSD(T). At the A5Z-CCSD(T) level the relative stabilization of $1^5\Delta$ compared to the $1^3\Pi$ decreases to 0.2 kcal mol^{-1}. However, the core electron correlated coupled cluster [*i.e.*, A5Z-C-CCSD(T)] switched the

Table 2 Dissociation energy with respect to Ta(^{4}F) + B(^{2}P) fragments (D_e, kcal mol^{-1}), bond length (r_e, Å), excitation energy (T_e, cm^{-1}), harmonic vibrational frequency (ω_e, cm^{-1}), and anharmonicity ($\omega_e x_e$, cm^{-1}) of 10 low-lying electronic states of TaB

State	Method[a]	D_e	r_e	T_e	ω_e	$\omega_e x_e$
$1^3\Pi$	A5Z-C-CCSD(T)	62.35	1.977	0	697	3.2
	A5Z-CCSD(T)	61.82	1.994	67	684	3.5
	CCSD(T)	60.67	1.996	238	682	3.5
	MRCI	62.37	2.012	0	663	3.7
	MRCI+Q	63.49	2.014	0	658	3.8
$1^5\Delta$	A5Z-C-CCSD(T)	61.65	2.120	242	582	2.4
	A5Z-CCSD(T)	62.01	2.141	0	586	2.9
	CCSD(T)	61.35	2.142	0	585	2.9
	MRCI	62.17	2.155	68	576	1.9
	MRCI+Q	63.27	2.156	76	573	2.1
$1^1\Sigma^+$	A5Z-C-CCSD(T)	59.80	1.943	890	656	2.6
	A5Z-CCSD(T)	59.41	1.959	911	662	2.9
	CCSD(T)	58.09	1.960	1141	662	3.0
	MRCI	57.88	1.966	1568	645	3.1
	MRCI+Q	59.35	1.968	1450	645	3.2
$1^5\Pi$	MRCI	57.42	1.998	1730	706	3.8
	MRCI+Q	58.78	2.001	1648	707	4.6
$1^5\Phi$	MRCI	55.68	1.999	2340	707	3.0
	MRCI+Q	57.07	2.002	2247	709	3.9
$1^3\Sigma^+$	MRCI	55.40	1.904	2438	774	4.8
	MRCI+Q	57.05	1.906	2254	764	4.5
$1^1\Pi$	MRCI	51.75	2.008	3713	655	5.3
	MRCI+Q	53.11	2.009	3630	650	5.0
$2^3\Pi$	MRCI	50.35	2.072	4203	605	7.2
	MRCI+Q	51.85	2.071	4072	606	6.8
$1^3\Phi$	MRCI	50.09	2.076	4292	572	−0.4
	MRCI+Q	51.59	2.075	4164	575	−0.3
$1^3\Sigma^-$	MRCI	50.07	2.121	4300	592	3.3
	MRCI+Q	51.77	2.123	4101	597	3.7

[a] Davidson corrected MRCI is given as MRCI+Q. The cc-pVQZ-PP (60ECP) of Ta and cc-pVQZ of B basis set was applied for all MRCI, MRCI+Q, and CCSD(T) calculations. The aug-cc-pV5Z-PP (60ECP) of Ta and aug-cc-pV5Z of B basis set used coupled cluster calculations are labeled as A5Z-CCSD(T). The $5s^25p^6$ (of Ta) core electrons correlated coupled cluster calculations performed with aug-cc-pwCV5Z-PP (60ECP) of Ta and aug-cc-pV5Z of B set are denoted by A5Z-C-CCSD(T).

ground state prediction to a 0.7 kcal mol^{-1} more stable $1^3\Pi$ compared to the $1^5\Delta$, which also agrees with the MRCI and MRCI+Q prediction. Under all utilized levels of theory, the D_e of $1^3\Pi$ and $1^5\Delta$ are ∼60.5–63.5 kcal mol^{-1} (Table 2). For all states MRCI+Q predicted 1–2 kcal mol^{-1} higher D_es compared to the MRCI D_es (Table 2).

The r_e values of the $1^3\Pi$, $1^5\Delta$, and $1^1\Sigma^+$ states decreased moving from CCSD(T) to A5Z-CCSD(T) to A5Z-C-CCSD(T), and the observation that the core electron correlation tends to contract the r_es is consistent with our previous findings on diatomic species.[37,41,88] The MRCI and MRCI+Q predicted slightly longer r_e values compared to CCSD(T) (by 0.01–0.02 Å) and the discrepancy between MRCI and MRCI+Q r_e predictions is less than 0.004 Å. Overall, at the MRCI level, the observed order of the electronic states of TaB is $1^3\Pi$, $1^5\Delta$, $1^1\Sigma^+$, $1^5\Pi$, $1^5\Phi$, $1^3\Sigma^+$, $1^1\Pi$, $2^3\Pi$, $1^3\Phi$, and $1^3\Sigma^-$. The MRCI+Q order is the same as MRCI except for the slightly stabilized $1^3\Sigma^-$ over the $1^3\Phi$ (by 63 cm^{-1}) (Table 2).

In the present work we have performed a spin–orbit analysis for the Ta atom to evaluate its splitting and to compare our results with the experimental literature values. Our calculated MRCI values and the experimental values are listed in the ESI,† Table S1. In line with the experimental values, MRCI predicted $a^4F_{3/2}$, $a^4F_{5/2}$, $a^4F_{7/2}$, and $a^4F_{9/2}$ ordering for the spin–orbit products of the a^4F of Ta. Importantly, for these states, the maximum discrepancy between MRCI *versus* experiment is only 183 cm^{-1}. The order of the spin–orbit constituents of the a^4P at the MRCI level is $a^4P_{3/2}$ (at 6559 cm^{-1}), $a^4P_{1/2}$ (at 6774 cm^{-1}), and $a^4P_{5/2}$ (at 10 112 cm^{-1}) which deviates from their experimental placements by 490, 725, and 859 cm^{-1}, respectively.[85] The excitation energies for the J = 7/2 and 9/2 of a^2G and J = 3/2 and 1/2 of a^6D are also calculated and given in the ESI† Table S1. Overall, we observed the deviations between experiment *versus* MRCI become significant moving to high energy states of Ta. Then, we investigated the spin–orbit splitting of the TaB. At the MRCI level, the 10 lowest energy electronic states of TaB were included in the spin–orbit matrix. The several low-lying spin–orbit curves resulting from these states are shown in Fig. 3. As expected, the spin–orbit effects of TaB are significant. The spin–orbit ground state of TaB is an $\Omega = 0^+$ which carries 56% $1^5\Delta$ + 31% $1^3\Pi$ + 5% $2^3\Pi$ + 7% $1^1\Sigma^+$ + 1% $1^3\Sigma^-$ components. The ground $\Omega = 0^+$ of TaB has a 61.14 kcal mol^{-1} D_e with respect to the lowest energy Ω state of TaB at r = 200 Å and its D_0 (with the zero-point energy) is 60.40 kcal mol^{-1}. The recently experimentally measured D_0 of TaB by Merriles *et al.*, is 2.700(3) eV (or ∼62.3 kcal mol^{-1}) and only 1.9 kcal mol^{-1} higher than our D_0.[31] The r_e of the spin–orbit corrected ground state of TaB ($\Omega = 0^+$) is slightly shorter than the r_e of $1^5\Delta$ of TaB (2.118 *versus* 2.155 Å). The calculated ω_e (519 cm^{-1}) and $\omega_e x_e$ (2.3 cm^{-1}) of the ground $\Omega = 0^+$ differ by 60 and 0.4 cm^{-1} from the corresponding values of the $1^5\Delta$. The second lowest energy $\Omega = 0^-$ has a mixing of 81% $1^5\Delta$ + 17% $1^3\Pi$ + 2% $2^3\Pi$ and lies approximately 1 kcal mol^{-1} above the ground $\Omega = 0^+$ state. The next several spin–orbit states of TaB are Ω = 1, 2, 1, 0^+, 0^-, 2,

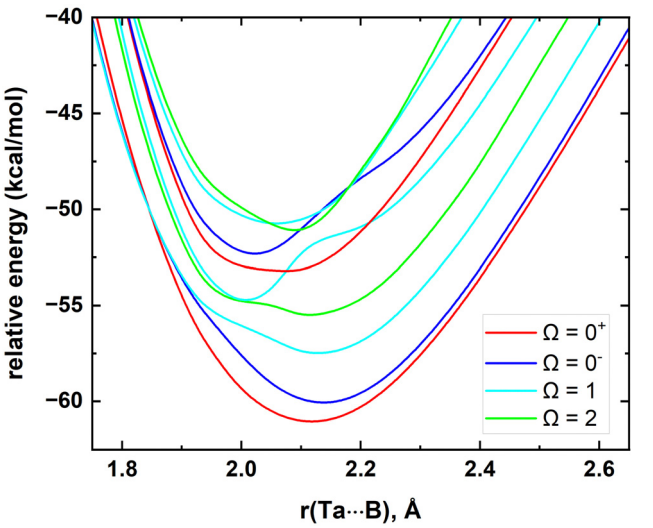

Fig. 3 Low-lying spin–orbit coupling curves of TaB as a function of Ta···B distance [r(Ta···B), Å]. The relative energies are referenced to the energy of the lowest Ω state of Ta(^{4}F) + B(^{2}P) fragments at r = 200 Å, which is set to 0 kcal mol^{-1}. The $\Omega = 0^+$, $\Omega = 0^-$, Ω = 1, and Ω = 2 curves are shown in red, blue, cyan, and green, respectively.

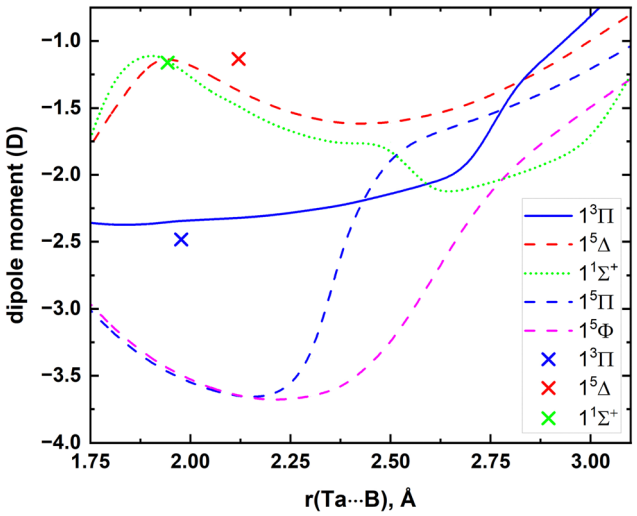

Fig. 4 MRCI DMCs of the lowest 5 electronic states of TaB as a function of Ta···B distance [r(Ta···B), Å]. The μ values of $1^3\Pi$, $1^5\Delta$, and $1^1\Sigma^+$ obtained under the A5Z-C-CCSD(T) level at their r_es are shown in blue (at −2.48 D), red (at −1.14 D), and green (at −1.16 D) cross marks, respectively.

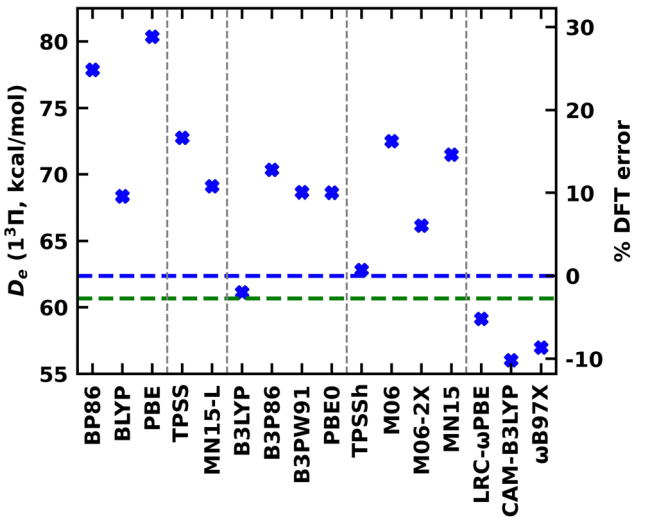

Fig. 5 Dissociation energy (D_e, in kcal mol^{-1}) of TaB($1^3\Pi$) obtained at various DFA with respect to Ta(^{4}F) + B(^{2}P) fragments (blue cross marks). The families of density functionals are separated with vertical gray dashed lines and ordered by the rung on the Jacob's ladder of DFA (left to right: GGA, MGGA, global GGA hybrid, MGGA hybrid, and RSH). The horizontal blue and green dashed lines represent MRCI and CCSD(T) D_es. The % DFT error is calculated with respect to the MRCI D_e.

and 1 which span 1238–3599 cm^{-1}. More information on the spin–orbit states of TaB is given in the ESI† Table S2.

The MRCI DMCs calculated for the 5 lowest electronic states of TaB are illustrated in Fig. 4. The μ values of single-reference $1^3\Pi$, $1^5\Delta$, and $1^1\Sigma^+$ states were also calculated at CCSD(T) and A5Z-C-CCSD(T) levels at their corresponding r_e values. Specifically, the CCSD(T) μ values of the aforementioned states are −2.54, −1.24, and −1.19 D, respectively, whereas those at the A5Z-C-CCSD(T) level are −2.48, −1.14, and −1.16 D. The calculated A5Z-C-CCSD(T) μ value is also marked in Fig. 4. The best harmony between MRCI *versus* A5Z-C-CCSD(T) was observed for the $1^1\Sigma^+$ state, whereas the μ values of $1^3\Pi$ and $1^5\Delta$ under the two theories are also in reasonable agreement (Fig. 4).

Going a step further, the single-reference $1^3\Pi$ electronic state of TaB was studied using a series of exchange–correlation functionals that span multiple rungs of the Jacob's ladder of DFA. The calculated D_e, r_e, ω_e, and $\omega_e x_e$ values under the GGA (BP86, BLYP, and PBE), MGGA (TPSS and MN15-L), global GGA hybrid (B3LYP, B3P86, B3PW91, and PBE0), MGGA hybrid (TPSSh, M06, M06-2X, and MN15), and RSH (LRC-ωPBE, CAM-B3LYP, and ωB97X) functionals are listed in the ESI,† Table S3. Generally, we expect the accuracy of the predictions to improve moving from less expensive GGA to more complex RSH functionals. As expected, the largest discrepancies between WFT D_es *versus* DFT D_es are displayed by the cheaper GGA PBE and BP86 (Fig. 5 and ESI,† Table S3). Specifically, these functionals overestimated the D_es by 18.0 and 15.5 kcal mol^{-1} (or by 29 and 25%), with respect to MRCI D_e, respectively (Fig. 5 and ESI,† Tables S3 and S4). Comparatively, the performance of the GGA BLYP is better with an error of ∼10%. The D_e errors of MGGA TPSS and MN15-L are larger than GGA BLYP but significantly lower than the GGA PBE and BP86. The global GGA hybrids consistently overestimated the D_e of TaB($1^3\Pi$) by 10–13% except for B3LYP which predicted a very similar D_e to the MRCI D_e (61.13 *versus* 62.37 kcal mol^{-1}). The harmony of D_e between B3LYP *vs* the CCSD(T) is even better (61.13 *versus* 60.67 kcal mol^{-1}). Among all the implemented functionals, the MGGA TPSSh carries the least error (less than 1%) for D_e. All RSH functionals underestimated the D_e of TaB($1^3\Pi$) by ∼5–10%. All functionals predicted shorter r_es compared to the MRCI. Compared to MRCI, the largest deviation was observed for the LRC-ωPBE (2.012 *versus* 1.862 Å). All other functionals predicted r_es of 1.92–2.00 Å with less than 5% errors (ESI,† Tables S3 and S4). Similar to r_e, the largest mismatch of DFT ω_e *versus* MRCI ω_e was produced by the LRC-ωPBE (663 *versus* 844 cm^{-1}), whereas all other functionals overestimated the ω_e by 10–90 cm^{-1} (Table 3). The DFT $\omega_e x_e$ values varied between 2.5–7.0 cm^{-1}, and the expensive RSH CAM-B3LYP and ωB97X predicted identical values to the MRCI $\omega_e x_e$ (Table 2 and ESI,† Table S3).

III.B. WB

The spin–orbit splitting of W is quite substantial; for example the J = 1–4 components of its ^{5}D ($5d^46s^2$) ground electronic state span from ∼4.8 to 17.8 kcal mol^{-1}.[85] The first electronically excited state of W (*i.e.*, ^{7}S) has a $5d^56s^1$ electron configuration and rests in between J = 1 and J = 2 components of the ^{5}D (specifically, the ^{7}S is at 8.4 kcal mol^{-1}).[85] The following two states of W (*i.e.*, ^{3}P and ^{3}H) carry the same electron configuration as the ground state and extend over 27.2–55.0 and 34.8–48.6 kcal mol^{-1}, respectively.[85]

In the present work, we have investigated the interaction of ^{5}D, ^{7}S, ^{3}P and ^{3}H electronic states of W with the B(^{2}P). According to the Wigner–Witmer rules, the interaction between W(^{5}D) + B(^{2}P), W(^{7}S) + B(^{2}P), W(^{3}P) + B(^{2}P), and W(^{3}H) + B(^{2}P) produces 15(sextet + quartet), 3(octet + sextet), 9(quartet + doublet), and

Table 3 Dominant electronic configurations of the 14 reported electronic states of WB

State[a]	Coefficient[b]	1σ	2σ	3σ	$1\pi_x$	$1\pi_y$	$1\delta_{x^2-y^2}$	$1\delta_{xy}$
$1^6\Pi$	0.91	2	α	α	2	α	α	α
$1^6\Sigma^+$	0.92	2	2	α	α	α	α	α
$1^4\Delta$	0.89	2	α	α	2	2	α	0
$1^2\Sigma^+$	0.84	2	2	α	2	2	0	0
	−0.21	2	0	α	2	2	0	2
	−0.21	2	0	α	2	2	2	0
$1^4\Pi$	0.55	2	2	α	2	α	0	α
	−0.55	2	2	α	α	2	α	0
	−0.24	2	β	α	2	α	α	α
$1^2\Delta$	0.69	2	α	β	2	2	α	0
	−0.27	2	β	α	2	2	α	0
	−0.42	2	α	α	2	2	β	0
$1^4\Phi$	0.61	2	2	α	2	α	0	α
	0.61	2	2	α	α	2	α	0
$2^4\Pi$	0.67	2	α	β	2	α	α	α
	−0.26	2	α	α	2	α	β	α
	−0.26	2	α	α	2	α	α	β
	0.24	2	2	0	2	α	α	α
$2^6\Sigma^+$	0.87	2	α	2	α	α	α	α
$1^2\Phi$	0.47	2	2	α	α	2	β	0
	0.47	2	2	α	2	α	0	β
	−0.37	2	2	β	2	α	0	α
	−0.37	2	2	β	α	2	α	0
$1^2\Pi$	0.33	2	2	α	α	2	β	0
	−0.33	2	2	α	2	α	0	β
	0.45	2	2	β	2	α	0	α
	−0.45	2	2	β	α	2	α	0
$3^4\Pi$	0.53	2	α	2	2	α	0	α
	−0.53	2	α	2	α	2	α	0
	−0.26	2	0	2	2	α	α	α
$2^4\Delta$	0.81	2	2	2	α	α	0	α
$2^2\Delta$	0.79	2	2	0	2	2	α	0

[a] Only the B_1 component of Π and Φ states and the A_1 component of Δ states under C_{2v} symmetry are listed. [b] Only the configuration interaction coefficients that are larger than 0.20 of the corresponding natural orbital representations are listed.

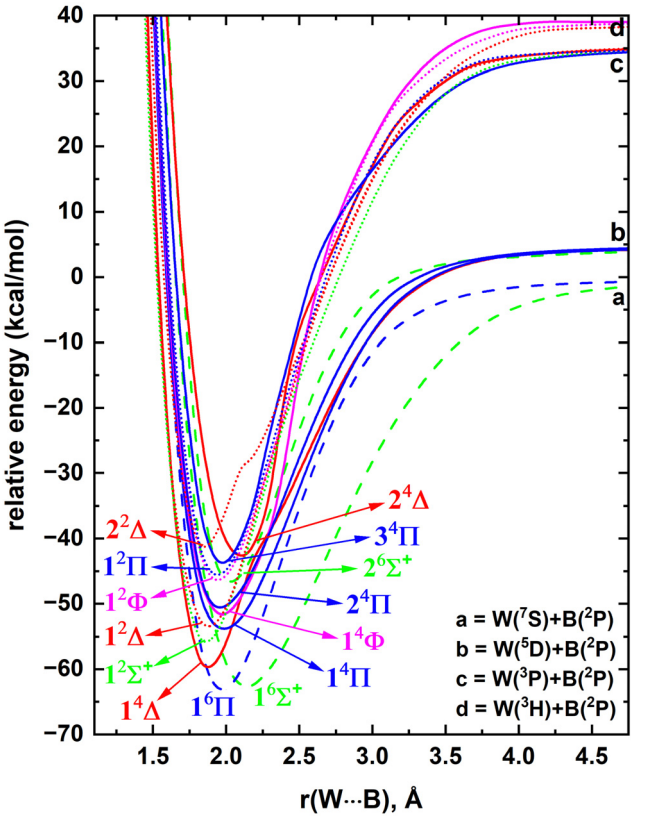

Fig. 6 Full MRCI PECs of WB as a function of W···B distance [r(W···B), Å]. The relative energies are referenced to the total energy of the W(7S) + B(2P) fragments at r = 200 Å, which is set to 0 kcal mol^{-1}. The Σ^+, Π, Δ, and Φ states are shown in green, blue, red, and pink, respectively. The solid, dotted, and dashed PECs represent quartet, doublet, and sextet spins, respectively.

33(quartet + doublet) spin states.[89,90] First, at the CASSCF level, all PECs originating from W(5D) + B(2P), W(7S) + B(2P), and W(3P) + B(2P) and a few more curves resulting from W(3H) + B(2P) were analyzed. Similar to TaB, WB bears a plethora of closely lying electronic states (ESI,† Fig. S2). The PECs of the most stable 14 electronic states of WB were plotted at the MRCI level and are illustrated in Fig. 6. At this level W(7S) + B(2P) is ∼5 kcal mol^{-1} more stable compared to the W(5D) + B(2P) fragments. This is not surprising since W(7S) and W(5D) are rather close in energy and importantly the produced MRCI potential energy profile (Fig. 6) does not account for spin–orbit effects. Indeed the stabilization of W(7S) compared to W(5D) has also been observed before by Ma and Balasubramanian under the CASSCF/SOCI (SOCI = second-order configuration interaction) level.[91]

According to our MRCI potential energy profile, the ground state of WB is a $^6\Pi$ originating from W(7S) + B(2P) fragments (Fig. 6). The $^6\Sigma^+$ state resulting from the same fragments is the first excited state of WB which lies energetically closer to the $^6\Pi$ state. The PEC of the second excited state of WB (*i.e.*, $1^4\Delta$) dissociates to W(5D) + B(2P) but an avoided crossing was observed at ∼2.2 Å with the $2^4\Delta$ PEC stemming from W(3P) + B(2P). The only $^2\Sigma^+$ state produced by W(3P) + B(2P) is in fact the next electronic state of WB (*i.e.*, $1^2\Sigma^+$). The proceeding 10 electronic states are amassed within ∼12 kcal mol^{-1} (Fig. 6) which clearly apprise of the complexity of the excited state spectrum of the molecule.

The dominant equilibrium electron configurations and the corresponding configuration interaction coefficients of the studied 14 electronic states of WB are listed in Table 3. The $1^6\Pi$ state carries the $1\sigma^2 2\sigma^1 3\sigma^1 1\pi^3 1\delta^2$ electron distribution. The electron configuration of $1^6\Sigma^+$ can be formed by transferring an electron from the $1^6\Pi$ state's doubly occupied 1π to its singly occupied 2σ. On the other hand, transferring an electron from the $1^6\Pi$ state's 1δ to its singly occupied 1π orbital creates $1^4\Delta$. $1^2\Sigma^+$ has minor multireference characteristics but with a major allocation of $1\sigma^2 2\sigma^2 3\sigma^1 1\pi^4$. Interestingly, among all studied states, $1^2\Sigma^+$ is the only state with a dominant configuration that does not host electrons in either of the δ orbitals (Table 3). Next 4 electronic states of WB (*i.e.*, $1^4\Pi$, $1^2\Delta$, $1^4\Phi$, $2^4\Pi$) exhibit rich multireference characters. Notice that $2^4\Pi$ has a similar electronic configuration to the ground state, $1^6\Pi$, where the spin up electrons in the 3σ and 1δ of the latter couple in different ways to produce the configuration of the former (note: only the three largest components of the $2^4\Pi$ were considered). The significant destabilization of the low spin $2^4\Pi$ compared to the $1^6\Pi$

(by ~13 kcal mol^{-1}; Fig. 6) is an example of the Hund's rule (recall that in the previous section we identified the $1^3\Pi$ and $1^1\Pi$ states of TaB as obeying the Hund rule). The heavy multireference nature of the low-spin open-shell electronic states is rather common especially for highly correlated systems with dense electronic spectra. The $1^2\Phi$ and $1^2\Pi$ of WB are two such states made of 4 distinct electron distributions (Table 3).

Upon comparing electronic structures of WB with TaB, the electron configuration of WB($1^6\Pi$) can be produced by attaching an electron to the vacant 1δ orbital of TaB($1^5\Pi$) (Tables 1 and 3). Similarly, the electronic configuration of WB($1^6\Sigma^+$) is formed by adding an electron to the empty 1δ of TaB($1^5\Delta$). Since the additional electron is being attached to a nonbonding 1δ orbital of TaB, approximately similar r_e values can be expected for WB($1^6\Pi$) *versus* TaB($1^5\Pi$) and WB($1^6\Sigma^+$) *versus* $1^5\Delta$(TaB). Indeed, the r_e values of WB($1^6\Sigma^+$) and $1^5\Delta$(TaB) are very similar (*i.e.*, 2.150 *versus* 2.155 Å, respectively) (Tables 2 and 4). On the other hand, the r_es of WB($1^6\Pi$) and TaB($1^5\Pi$) are 1.971 and 2.001 Å, respectively. This slightly longer r_e of the latter compared to the former (by 0.03 Å) might be a result of its multireference nature.

The MRCI and MRCI+Q D_es of the 14 electronic states of WB calculated with respect to W(^{7}S) + B(^{2}P) dissociation is reported in Table 4. The differences between MRCI and MRCI+Q D_es are less than 1 kcal mol^{-1}. At the MRCI level the D_e of WB ($1^6\Pi$) is 63.32 kcal mol^{-1} with respect to the W(^{7}S) + B(^{2}P) asymptote. The zero-point energy correction decreased this value to 62.38 kcal mol^{-1}. The experimental D_0 of the WB reported by Merriles *et al.*, is 2.730(4) eV (or ~63 kcal mol^{-1}).[31] Importantly, recall that the experimental ground state of W is ^{5}D and hence we cannot make direct comparisons between our MRCI or MRCI+Q values *versus* the experimentally measured D_0 by Merriles *et al.* However, a series of corrections can be made to predict its D_0 with respect to W(^{5}D) + B(^{2}P) from the D_0 calculated with reference to the W(^{7}S) + B(^{2}P) fragments. For example, an *ab initio* analysis reported for the first three electronic states of WB (*i.e.*, $1^6\Pi$, $1^6\Sigma^+$, $1^4\Delta$), incorporated a series of corrections (see ref. 12) to attain a D_0 of 2.67 eV (or 61.57 kcal mol^{-1}) for WB ($1^6\Pi$) with respect to the W(^{5}D) + B(^{2}P) fragments, which is in harmony with the experimental D_0 by Merriles *et al.*[31]

The ~0.2 Å long bond distance of $1^6\Sigma^+$ compared to $1^6\Pi$ (Table 4) can be rationalized by their electron arrangements or bond orders. Specifically, the approximate bond orders of these two states are 1.5 and 2, respectively. The approximate bond orders of both $1^4\Delta$ and $1^2\Sigma^+$ are 2.5 and as expected their r_es (1.876 and 1.859 Å, respectively at MRCI) are shorter than both $1^6\Pi$ and $1^6\Sigma^+$. The CCSD(T) r_es reported for the $1^6\Pi$, $1^6\Sigma^+$, and $1^4\Delta$ states by Melo and Dixon are 1.952, 2.117, and 1.856 Å, respectively.[12] For all three states our MRCI and MRCI+Q r_e values are ~0.019–0.033 Å longer compared to their CCSD(T) values. This observation of slightly longer MRCI and MRCI+Q r_es compared to CCSD(T) r_es is in line with our findings of TaB.

For all states MRCI predicted 16–360 cm^{-1} higher excitation energies compared to MRCI+Q, except for the $1^2\Pi$ that has a slightly lower MRCI excitation energy (only by 11 cm^{-1}) compared to the MRCI+Q (Table 4). Overall, at the MRCI level, the obtained order of the electronic states of WB is $1^6\Pi$, $1^6\Sigma^+$, $1^4\Delta$, $1^2\Sigma^+$, $1^4\Pi$, $1^2\Delta$, $1^4\Phi$, $2^4\Pi$, $2^6\Sigma^+$, $1^2\Phi$, $1^2\Pi$, $3^4\Pi$, $2^4\Delta$, $2^2\Delta$. MRCI+Q follows the same order except for the 172 cm^{-1} stable $1^2\Delta$ over the $1^4\Pi$.

Next, we performed spin–orbit analysis for the W atom and the WB molecule. Our calculated spin–orbit splitting and the experimental literature values of W are given in the ESI† Table S5. The ^{5}D ground state of W produces five spin–orbit products (J = 0, 1, 2, 3, 4). Experimentally the J = 3 of the first excited ^{7}S falls in between the J = 1 and 2 of ^{5}D.[85] However, MRCI predicted the $^7S_3$ to be in between $^5D_2$ and $^5D_3$ (ESI,† Table S5). The largest discrepancy observed between MRCI *versus* experiment is less than 460 cm^{-1}. All 14 low-lying electronic states of WB were included in the spin–orbit matrix to study the spin–orbit effects of WB. At r_e = 1.971 Å (which is the r_e of $1^6\Pi$ at MRCI), the order of the lowest Ω states of WB is 7/2, 5/2, 3/2, 1/2, 1/2, 1/2, and 3/2. The ground Ω = 7/2 is dominantly $1^6\Pi$ (91%) with a minor fraction of $1^4\Delta$ (9%). These values of Ω = 7/2 are in excellent agreement with the values reported in the recent work by Melo and Dixon.[12] Our calculated compositions of all the Ω states are listed in the ESI† Table S6. Importantly, the spin–orbit coupling effects of WB are significant and for example, the first four spin–orbit states of WB are contained within 113 cm^{-1} (ESI,† Table S6). Another

Table 4 Dissociation energy with respect to W(^{7}S) + B(^{2}P) fragments (D_e, kcal mol^{-1}), bond length (r_e, Å), excitation energy (T_e, cm^{-1}), harmonic vibrational frequency (ω_e, cm^{-1}), and anharmonicity ($\omega_e x_e$, cm^{-1}) of the 14 low-lying electronic states of WB

State	Method[a]	D_e	r_e	T_e	ω_e	$\omega_e x_e$
$1^6\Pi$	MRCI	63.32	1.971	0	718	4.0
	MRCI+Q	63.20	1.975	0	715	4.3
$1^6\Sigma^+$	MRCI	62.62	2.150	245	555	3.5
	MRCI+Q	62.62	2.140	204	559	3.8
$1^4\Delta$	MRCI	60.00	1.876	1160	823	3.3
	MRCI+Q	60.16	1.877	1063	820	3.7
$1^2\Sigma^+$	MRCI	56.11	1.859	2523	807	4.8
	MRCI+Q	56.20	1.861	2446	813	6.0
$1^4\Pi$	MRCI	53.92	1.983	3286	567	1.5
	MRCI+Q	53.99	1.987	3219	573	1.9
$1^2\Delta$	MRCI	53.75	1.879	3348	712	3.1
	MRCI+Q	54.49	1.874	3047	705	2.3
$1^4\Phi$	MRCI	51.77	1.970	4040	681	8.1
	MRCI+Q	52.09	1.970	3886	693	7.7
$2^4\Pi$	MRCI	50.74	1.956	4401	629	8.3
	MRCI+Q	50.66	1.962	4385	587	7.4
$2^6\Sigma^+$	MRCI	46.76	2.030	5790	738	6.3
	MRCI+Q	47.16	2.034	5609	712	4.3
$1^2\Phi$	MRCI	46.43	1.941	5906	740	3.9
	MRCI+Q	46.47	1.943	5849	739	4.5
$1^2\Pi$	MRCI	45.77	1.940	6137	745	3.8
	MRCI+Q	45.62	1.942	6148	744	3.7
$3^4\Pi$	MRCI	43.69	1.978	6864	824	5.3
	MRCI+Q	44.59	1.976	6508	820	5.8
$2^4\Delta$	MRCI	42.50	2.113	7281	680	5.0
	MRCI+Q	42.94	2.112	7085	668	4.2
$2^2\Delta$	MRCI	41.71	1.844	7559	863	4.8
	MRCI+Q	42.61	1.845	7199	860	4.0

[a] Davidson corrected MRCI is given as MRCI+Q. The cc-pVQZ-PP (60ECP) of W and cc-pVQZ of B basis set was applied for all MRCI and MRCI+Q calculations.

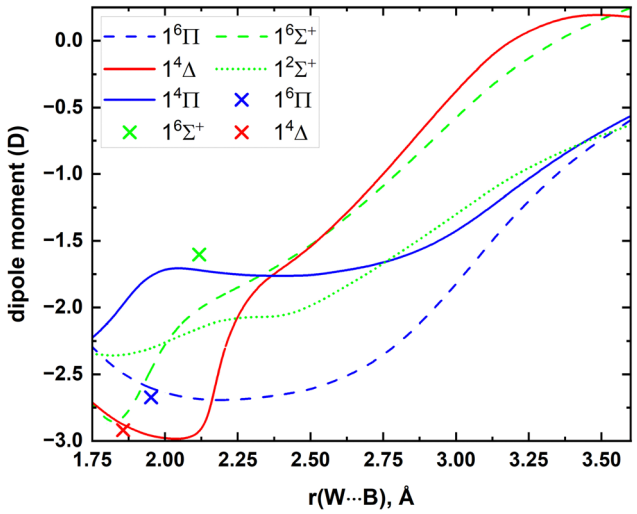

Fig. 7 MRCI DMCs of the lowest 5 electronic states of WB as a function of W···B distance [r(W···B), Å]. The μ values of $1^6\Pi$, $1^6\Sigma^+$, and $1^4\Delta$ obtained under the A5Z-C-CCSD(T) level at their r_es are shown in blue (at −2.67 D), green (at −1.60 D), and red (at −2.92 D) cross marks, respectively. The CCSD(T) r_es reported by Melo and Dixon were used to calculate the A5Z-C-CCSD(T) μ values.[12]

spin–orbit calculation was performed at r_e = 2.150 Å, which is the MRCI r_e of the $1^6\Sigma^+$ state of WB. At this distance, the lowest energy spin–orbit state of WB is an Ω = 5/2 with 90% $1^6\Sigma^+$ and 9% $1^4\Pi$. The other two spin–orbit components of $1^6\Sigma^+$ (*i.e.*, Ω = 3/2 and 1/2), lie 156 and 184 cm^{-1} above the $1^6\Sigma^+{}_{1/2}$. Importantly, even though the $1^6\Sigma^+$ lies only 245 cm^{-1} above $1^6\Pi$ (Table 4) the $1^6\Sigma^+{}_{5/2}$ lies 641 cm^{-1} above the $1^6\Pi_{7/2}$. This confirms that the ground state of WB is indeed the $1^6\Pi_{7/2}$.

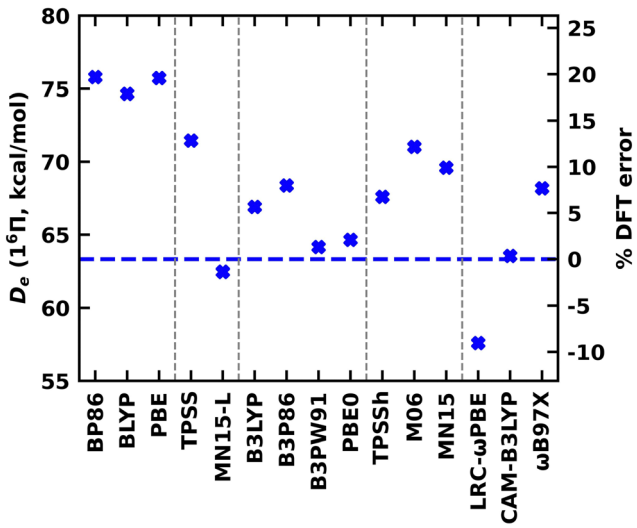

Fig. 8 Dissociation energy (D_e, in kcal mol^{-1}) of WB($1^6\Pi$) obtained at various DFA (blue cross marks) with respect to the W(^{7}S) + B(^{2}P) fragments. The families of density functionals are separated with vertical gray dashed lines and ordered by the rung on the Jacob's ladder of DFA (left to right: GGA, MGGA, global GGA hybrid, MGGA hybrid, and RSH). The horizontal blue dashed line represents the MRCI D_e.

To the best of our knowledge, the μ values or DMCs of WB are not available in the literature. Hence, at the MRCI level the DMCs were produced and plotted in Fig. 7. The A5Z-C-CCSD(T) μ values for the single-reference $1^6\Pi$, $1^6\Sigma^+$, and $1^4\Delta$ states were also calculated at their r_es and they are −2.67, −1.60, and −2.92 D, respectively (for comparison these values are also marked in Fig. 7). The MRCI and A5Z-C-CCSD(T) μ values of the $1^6\Pi$ and $1^4\Delta$ states agree well with each other, but the discrepancy between the two levels for the $1^6\Sigma^+$ is ∼0.4 D.

A DFT analysis was also conducted for the $1^6\Pi$ and $1^4\Delta$ states of WB. The DFT values calculated under various exchange–correlation functionals are reported in the ESI† Table S7. The % DFT errors calculated with respect to the MRCI values are given in the ESI† Tables S8 and S9. Note that all DFT D_es reported for the $1^6\Pi$ and $1^4\Delta$ are with respect to the W(^{7}S) + B(^{2}P) dissociation. The DFT D_es of the $1^6\Pi$ and $1^4\Delta$ states of WB are also shown in Fig. 8 and the ESI† Fig. S3, respectively. Similar to TaB($1^3\Pi$), all GGA functionals overestimated the D_e of the $1^6\Pi$ and $1^4\Delta$ states of WB by 9–14 kcal mol^{-1} (with respect to MRCI D_e). Convergence issues were observed for the MGGA MN15-L calculation of $1^4\Delta$ and are not reported here. The MN15-L performance for the $1^6\Pi$ D_e is exceptional with less than 2% deviation from the MRCI D_e. All global GGA hybrid functionals predicted less than 9% errors for both $1^6\Pi$ and $1^4\Delta$. Among the MGGA hybrids, the TPSSh carried the minimal errors for the D_es for both states and specifically the TPSSh D_e of the $1^4\Delta$ state is almost identical to the MRCI value (60.33 *versus* 60.00 kcal mol^{-1}). Recall that we observed a better performance by the TPSSh for the D_e of TaB($1^3\Pi$) as well. The RSH CAM-B3LYP predicted D_e for both states of WB are in excellent agreement with the MRCI, but the other two RSH functionals (*i.e.*, LRC-ωPBE and ωB97X) carry errors of 7–19%. Overall, the global GGA hybrid B3LYP, MGGA hybrid TPSSh, and RSH CAM-B3LYP were found to represent the D_es of $1^3\Pi$ of TaB and $1^6\Pi$ and $1^4\Delta$ of WB accurately.

The DFT r_e values of $1^6\Pi$ and $1^4\Delta$ of WB have less than 0.05 Å deviation from the corresponding MRCI values (Table 4 and the ESI,† Table S7). Similar to TaB($1^3\Pi$), the deviation of LRC-ωPBE ω_e from the MRCI value is 20% greater for WB($1^4\Delta$), but it is only ∼5% for the WB($1^6\Pi$). The DFT $\omega_e x_e$ values of WB varied within 3.7–6.7 cm^{-1}. The better performing B3LYP, TPSSh, and CAM-B3LYP for D_e also showed smaller errors for ω_e (ESI,† Tables S8 and S9). Interestingly, the less expensive GGA functionals carried minor errors on $\omega_e x_e$ compared to the more expensive functionals.

IV. Conclusions

This work was devoted to investigating the low-lying electronic states of TaB and WB species. Specifically, 10 and 14 electronic states of TaB and WB respectively were analyzed utilizing high-level MRCI, MRCI+Q, and CCSD(T) levels of theory with the correlation-consistent basis sets. The full PECs, equilibrium electronic configurations, spectroscopic parameters, and several energy related properties for these states of TaB and

WB are reported. All studied electronic states of TaB and WB lie close in energy (within ~12 and 21 kcal mol^{-1}, respectively) and several of these are multireference in nature. The lowest-lying $1^3\Pi$ and $1^5\Delta$ states of TaB are energetically almost degenerate with ~62 kcal mol^{-1} D_e with reference to the Ta(^{4}F) + B(^{2}P) ground state fragments and their ordering is sensitive to the level of theory being utilized. Specifically, at the MRCI, MRCI+Q, and A5Z-C-CCSD(T) levels, $1^3\Pi$ ($1\sigma^2 2\sigma^2 3\sigma^1 1\pi^3$) is slightly stable over $1^5\Delta$ ($1\sigma^2 2\sigma^2 3\sigma^1 1\pi^2 1\delta^1$) but the ordering is the opposite at the CCSD(T) and A5Z-CCSD(T) levels. The spin–orbit analysis made at the MRCI level predicted the $1^5\Delta_0$ spin–orbit state to be the ground state of TaB. The zero-point energy corrected D_0 of the $1^5\Delta_0$ (*i.e.*, 60.4 kcal mol^{-1}) is in reasonable agreement with the experimentally measured D_0 of the TaB by Merriles *et al.* (*i.e.*, 62.3 kcal mol^{-1}).[31] Similar to TaB, the two most stable electronic states of WB are close in energy (*i.e.*, $1^6\Pi$ and $1^6\Sigma^+$ are separated only by ~0.6 kcal mol^{-1}) but both MRCI and MRCI+Q levels predicted the $1^6\Pi$ to be the ground electronic state. This is consistent with a previous *ab initio* analysis reported by Melo and Dixon.[12]

MRCI findings of the $1^3\Pi$ state of TaB and $1^6\Pi$ and $1^4\Delta$ states of WB were used to evaluate DFT errors on a series of functionals spanning GGA, MGGA, global GGA hybrid, MGGA hybrid, and RSH classes of functionals. Many functionals predicted DFT r_es with minimal errors. As a family, the less expensive GGA displayed large deviations for D_es with respect to MRCI. Among all functionals, the global GGA hybrid B3LYP, MGGA hybrid TPSSh, and RSH CAM-B3LYP predicted D_es and ω_es are in good agreement with the MRCI D_es. The more expensive functionals displayed larger errors for $\omega_e x_e$ compared to the cheaper GGAs. Our DFT analysis showcases the difficulty associated with choosing a specific functional for accurate representation of various properties of highly correlated inorganic species and that simply climbing the Jacob's ladder of DFA is not a guarantee for improved accuracy of the predictions for such systems.

Data availability

The data supporting this article have been included as part of the ESI.†

Conflicts of interest

There are no conflicts to declare.

Acknowledgements

The support of the Los Alamos National Laboratory (LANL) Laboratory Directed Research and Development program Project No. 20240737PRD1 is acknowledged. This research used resources provided by the Los Alamos National Laboratory Institutional Computing Program, which is supported by the U.S. Department of Energy National Nuclear Security Administration under Contract No. 89233218CNA000001. Prof. Evangelos Miliordos is thanked for the useful discussions about spin–orbit coupling effects.

References

1 G. F. de Melo, M. Vasiliu, G. Liu, S. Ciborowski, Z. Zhu, M. Blankenhorn, R. Harris, C. Martinez-Martinez, M. Dipalo, K. A. Peterson, K. H. Bowen and D. A. Dixon, *J. Phys. Chem. A*, 2022, **126**, 9392–9407.
2 G. Liu, Z. Zhu, S. M. Ciborowski, I. R. Ariyarathna, E. Miliordos and K. H. Bowen, *Angew. Chem., Int. Ed.*, 2019, **58**, 7773–7777.
3 G. Liu, I. R. Ariyarathna, S. M. Ciborowski, Z. Zhu, E. Miliordos and K. H. Bowen, *J. Am. Chem. Soc.*, 2020, **142**, 21556–21561.
4 G. Liu, I. R. Ariyarathna, Z. Zhu, S. M. Ciborowski, E. Miliordos and K. H. Bowen, *Phys. Chem. Chem. Phys.*, 2022, **24**, 4226–4231.
5 D. M. Merriles, A. London, E. Tieu, C. Nielson and M. D. Morse, *Inorg. Chem.*, 2023, **62**, 9589–9601.
6 M. D. Morse, *Chem. Rev.*, 2002, **86**, 1049–1109.
7 J. D. Mosley, J. W. Young, J. Agarwal, H. F. Schaefer, 3rd, P. Schleyer and M. A. Duncan, *Angew. Chem., Int. Ed.*, 2014, **53**, 5888–5891.
8 M. A. Duncan, *Rev. Sci. Instrum.*, 2012, **83**, 041101.
9 J. F. Harrison, *Chem. Rev.*, 2000, **100**, 679–716.
10 E. E. Claveau and E. Miliordos, *Phys. Chem. Chem. Phys.*, 2021, **23**, 21172–21182.
11 I. R. Ariyarathna and E. Miliordos, *Phys. Chem. Chem. Phys.*, 2019, **21**, 24469–24477.
12 G. F. de Melo and D. A. Dixon, *J. Phys. Chem. A*, 2023, **127**, 1588–1597.
13 I. R. Ariyarathna, *Phys. Chem. Chem. Phys.*, 2024, DOI: 10.1039/d4cp01847h.
14 Y. Gong, M. Zhou and L. Andrews, *Chem. Rev.*, 2009, **109**, 6765–6808.
15 E. E. Claveau, S. Sader, B. A. Jackson, S. N. Khan and E. Miliordos, *Phys. Chem. Chem. Phys.*, 2023, **25**, 5313–5326.
16 Y. W. Ng, H. F. Pang and A. S. Cheung, *J. Chem. Phys.*, 2011, **135**, 204308.
17 D. Tzeli and A. Mavridis, *J. Chem. Phys.*, 2008, **128**, 034309.
18 L. F. Ferrao, R. F. Spada, O. Roberto-Neto and F. B. Machado, *J. Chem. Phys.*, 2013, **139**, 124316.
19 A. C. Borin and J. P. Gobbo, *Int. J. Quantum Chem.*, 2011, **111**, 3362–3370.
20 D. Tzeli and I. Karapetsas, *J. Phys. Chem. A*, 2020, **124**, 6667–6681.
21 I. Cernusak, M. Dallos, H. Lischka, T. Muller and M. Uhlar, *J. Chem. Phys.*, 2007, **126**, 214311.
22 C. Demetriou, C. E. Tzeliou, A. Androutsopoulos and D. Tzeli, *Molecules*, 2023, **28**, 8016.
23 B. Welch, R. McLean and A. K. Wilson, *Mol. Phys.*, 2023, **121**, e2248292.
24 D. M. Merriles, E. Tieu and M. D. Morse, *J. Chem. Phys.*, 2019, **151**, 044302.
25 D. M. Merriles and M. D. Morse, *J. Phys. Chem. Lett.*, 2023, **14**, 7361–7367.
26 E. S. Goudreau, A. G. Adam, D. W. Tokaryk and C. Linton, *J. Mol. Spectrosc.*, 2015, **314**, 13–18.

27 W. J. Balfour, P. K. Chowdhury and R. Li, *Chem. Phys. Lett.*, 2008, **463**, 25–28.
28 J.-f Zhen, L. Wang, C.-b Qin, Q. Zhang and Y. Chen, *Chin. J. Chem. Phys.*, 2010, **23**, 626–629.
29 Y. W. Ng, H. F. Pang, Y. Qian and A. S. Cheung, *J. Phys. Chem. A*, 2012, **116**, 11568–11572.
30 L. F. Cheung, T. T. Chen, G. S. Kocheril, W. J. Chen, J. Czekner and L. S. Wang, *J. Phys. Chem. Lett.*, 2020, **11**, 659–663.
31 D. M. Merriles, C. Nielson, E. Tieu and M. D. Morse, *J. Phys. Chem. A*, 2021, **125**, 4420–4434.
32 A. C. Borin, J. P. Gobbo and C. A. Castro, *J. Mol. Model.*, 2014, **20**, 2285.
33 L. F. Cheung, G. S. Kocheril, J. Czekner and L. S. Wang, *J. Chem. Phys.*, 2020, **152**, 174301.
34 J. Ye, H. F. Pang, A. M. Wong, J. W. Leung and A. S. Cheung, *J. Chem. Phys.*, 2008, **128**, 154321.
35 Y. W. Ng, Y. S. Wong, H. F. Pang and A. S. Cheung, *J. Chem. Phys.*, 2012, **137**, 124302.
36 K. A. Gingerich, *J. Chem. Phys.*, 1971, **54**, 2646–2650.
37 I. R. Ariyarathna, C. Duan and H. J. Kulik, *J. Chem. Phys.*, 2022, **156**, 184113.
38 V. Kalamse, S. Gaikwad and A. Chaudhari, *Bull. Mater. Sci.*, 2010, **33**, 233–238.
39 H. Lischka, D. Nachtigallova, A. J. A. Aquino, P. G. Szalay, F. Plasser, F. B. C. Machado and M. Barbatti, *Chem. Rev.*, 2018, **118**, 7293–7361.
40 K. D. Vogiatzis, M. V. Polynski, J. K. Kirkland, J. Townsend, A. Hashemi, C. Liu and E. A. Pidko, *Chem. Rev.*, 2019, **119**, 2453–2523.
41 I. R. Ariyarathna and E. Miliordos, *Phys. Chem. Chem. Phys.*, 2018, **20**, 12278–12287.
42 N. M. S. Almeida, I. R. Ariyarathna and E. Miliordos, *J. Phys. Chem. A*, 2019, **123**, 9336–9344.
43 I. R. Ariyarathna, N. M. S. Almeida and E. Miliordos, *Phys. Chem. Chem. Phys.*, 2020, **22**, 16072–16079.
44 I. R. Ariyarathna and E. Miliordos, *J. Quant. Spectrosc. Radiat. Transfer*, 2020, **255**, 107265.
45 N. M. S. Almeida, I. R. Ariyarathna and E. Miliordos, *Phys. Chem. Chem. Phys.*, 2018, **20**, 14578–14586.
46 P. Geerlings, F. De Proft and W. Langenaeker, *Chem. Rev.*, 2003, **103**, 1793–1873.
47 A. D. Becke, *J. Chem. Phys.*, 2014, **140**, 18A301.
48 K. Burke, *J. Chem. Phys.*, 2012, **136**, 150901.
49 H. S. Yu, S. L. Li and D. G. Truhlar, *J. Chem. Phys.*, 2016, **145**, 130901.
50 W. Kohn, *Rev. Mod. Phys.*, 1999, **71**, 1253–1266.
51 I. R. Ariyarathna, Y. Cho, C. Duan and H. J. Kulik, *Phys. Chem. Chem. Phys.*, 2023, **25**, 26632–26639.
52 L. R. Maurer, M. Bursch, S. Grimme and A. Hansen, *J. Chem. Theory Comput.*, 2021, **17**, 6134–6151.
53 J. P. Perdew, Presented in part at the AIP Conference Proceedings, 2001.
54 H.-J. Werner and P. J. Knowles, *J. Chem. Phys.*, 1988, **89**, 5803–5814.
55 P. J. Knowles and H.-J. Werner, *Chem. Phys. Lett.*, 1988, **145**, 514–522.
56 K. R. Shamasundar, G. Knizia and H. J. Werner, *J. Chem. Phys.*, 2011, **135**, 054101.
57 K. Raghavachari, G. W. Trucks, J. A. Pople and M. Head-Gordon, *Chem. Phys. Lett.*, 1989, **157**, 479–483.
58 H. J. Werner, P. J. Knowles, G. Knizia, F. R. Manby and M. Schütz, *Wiley Interdiscip. Rev.: Comput. Mol. Sci.*, 2011, **2**, 242–253.
59 H. J. Werner, P. J. Knowles, F. R. Manby, J. A. Black, K. Doll, A. Hesselmann, D. Kats, A. Kohn, T. Korona, D. A. Kreplin, Q. Ma, T. F. Miller, 3rd, A. Mitrushchenkov, K. A. Peterson, I. Polyak, G. Rauhut and M. Sibaev, *J. Chem. Phys.*, 2020, **152**, 144107.
60 H.-J. Werner and P. J. Knowles, *et al.*, *MOLPRO, version 2023.2*, a package of ab initio programs, see **https://www.molpro.net**.
61 M. J. Frisch, G. W. Trucks, H. B. Schlegel, G. E. Scuseria, M. A. Robb, J. R. Cheeseman, G. Scalmani, V. Barone, G. A. Petersson, H. Nakatsuji, X. Li, M. Caricato, A. V. Marenich, J. Bloino, B. G. Janesko, R. Gomperts, B. Mennucci, H. P. Hratchian, J. V. Ortiz, A. F. Izmaylov, J. L. Sonnenberg, D. Williams, F. Ding, F. Lipparini, F. Egidi, J. Goings, B. Peng, A. Petrone, T. Henderson, D. Ranasinghe, V. G. Zakrzewski, J. Gao, N. Rega, G. Zheng, W. Liang, M. Hada, M. Ehara, K. Toyota, R. Fukuda, J. Hasegawa, M. Ishida, T. Nakajima, Y. Honda, O. Kitao, H. Nakai, T. Vreven, K. Throssell, J. A. Jr., J. E. Peralta, F. Ogliaro, M. J. Bearpark, J. J. Heyd, E. N. Brothers, K. N. Kudin, V. N. Staroverov, T. A. Keith, R. Kobayashi, J. Normand, K. Raghavachari, A. P. Rendell, J. C. Burant, S. S. Iyengar, J. Tomasi, M. Cossi, J. M. Millam, M. Klene, C. Adamo, R. Cammi, J. W. Ochterski, R. L. Martin, K. Morokuma, O. Farkas, J. B. Foresman and D. J. Fox, Gaussian Inc., Wallingford CT, 2016.
62 T. H. Dunning, *J. Chem. Phys.*, 1989, **90**, 1007–1023.
63 D. Figgen, K. A. Peterson, M. Dolg and H. Stoll, *J. Chem. Phys.*, 2009, **130**, 164108.
64 H.-J. Werner and P. J. Knowles, *J. Chem. Phys.*, 1985, **82**, 5053–5063.
65 P. J. Knowles and H.-J. Werner, *Chem. Phys. Lett.*, 1985, **115**, 259–267.
66 D. A. Kreplin, P. J. Knowles and H. J. Werner, *J. Chem. Phys.*, 2019, **150**, 194106.
67 D. A. Kreplin, P. J. Knowles and H. J. Werner, *J. Chem. Phys.*, 2020, **152**, 074102.
68 R. A. Kendall, T. H. Dunning and R. J. Harrison, *J. Chem. Phys.*, 1992, **96**, 6796–6806.
69 J. P. Perdew, *Phys. Rev. B: Condens. Matter Mater. Phys.*, 1986, **33**, 8822–8824.
70 A. D. Becke, *Phys. Rev. A*, 1988, **38**, 3098–3100.
71 B. Miehlich, A. Savin, H. Stoll and H. Preuss, *Chem. Phys. Lett.*, 1989, **157**, 200–206.
72 F. J. Devlin, J. W. Finley, P. J. Stephens and M. J. Frisch, *J. Phys. Chem.*, 1995, **99**, 16883–16902.
73 J. P. Perdew, K. Burke and M. Ernzerhof, *Phys. Rev. Lett.*, 1996, **77**, 3865–3868.
74 J. Tao, J. P. Perdew, V. N. Staroverov and G. E. Scuseria, *Phys. Rev. Lett.*, 2003, **91**, 146401.

75 H. S. Yu, X. He and D. G. Truhlar, *J. Chem. Theory Comput.*, 2016, **12**, 1280–1293.
76 A. D. Becke, *J. Chem. Phys.*, 1993, **98**, 5648–5652.
77 P. J. Stephens, F. J. Devlin, C. F. Chabalowski and M. J. Frisch, *J. Phys. Chem.*, 1994, **98**, 11623–11627.
78 C. Adamo and V. Barone, *J. Chem. Phys.*, 1999, **110**, 6158–6170.
79 M. Ernzerhof and G. E. Scuseria, *J. Chem. Phys.*, 1999, **110**, 5029–5036.
80 Y. Zhao and D. G. Truhlar, *Theor. Chem. Acc.*, 2007, **120**, 215–241.
81 H. S. Yu, X. He, S. L. Li and D. G. Truhlar, *Chem. Sci.*, 2016, **7**, 5032–5051.
82 M. A. Rohrdanz, K. M. Martins and J. M. Herbert, *J. Chem. Phys.*, 2009, **130**, 054112.
83 T. Yanai, D. P. Tew and N. C. Handy, *Chem. Phys. Lett.*, 2004, **393**, 51–57.
84 J. D. Chai and M. Head-Gordon, *J. Chem. Phys.*, 2008, **128**, 084106.
85 A. Kramida, Y. Ralchenko and J. Reader, *NIST Atomic Spectra Database (Version 5.3)*, National Institute of Standards and Technology, Gaithersburg, MD, 2015, **https://physics.nist.gov/asd**.
86 M. D. Hanwell, D. E. Curtis, D. C. Lonie, T. Vandermeersch, E. Zurek and G. R. Hutchison, *J. Cheminf.*, 2012, **4**, 17.
87 Avogadro: an open-source molecular builder and visualization tool, Version 1.2.0 edn.
88 I. R. Ariyarathna and E. Miliordos, *J. Quant. Spectrosc. Radiat. Transfer*, 2022, **280**, 108074.
89 R. S. Mulliken, *Rev. Mod. Phys.*, 1932, **4**, 1–86.
90 E. Wigner and E. E. Witmer, *Z. Phys.*, 1928, **51**, 859–886.
91 Z. Ma and K. Balasubramanian, *Chem. Phys. Lett.*, 1991, **181**, 467–473.